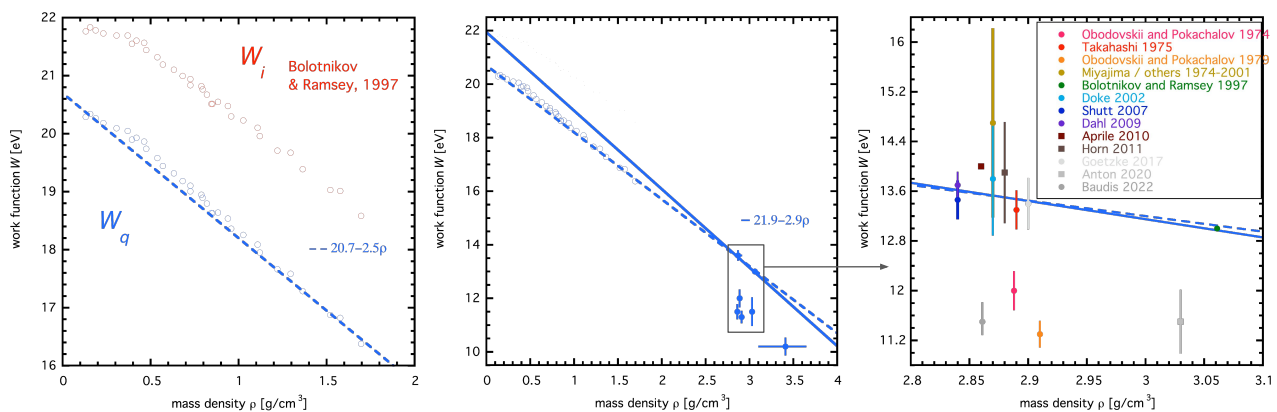


## Supplementary Material

### 1 APPENDIX A: WORK FUNCTION, EXCITON-ION RATIO, AND FANO FACTOR

This appendix presents the origins of the density-dependent work function for total quanta  $W_q$  and the high- $E$  asymptote of the exciton-to-ion ratio  $N_{ex}/N_i$  implemented within NEST, as well as the Fano-like factor for total quanta, all for ER. Note that Figure S1 uses a 21.8 eV normalization for  $W_i$ , reported as going to 1.00 as  $\rho \rightarrow 0$  g/cm<sup>3</sup> in [1] and [2]. That value is based upon averaging three values reported in the same sources without recorded error bars: 21.5 and 22.1 (originally from [3], and also the ICRU value) in the former source and 21.9 in the latter. It represents  $1/Q_y$  as  $\mathcal{E} \rightarrow \infty$ . ( $W_q < W_i$  by definition.)



**Figure S1.** Left: The ionization work function,  $W_i$ , as a function of the density for GXe (gaseous Xe) as hollow red circles [2] normalized to  $W_{i,0} = 21.8$  eV, and converted to  $W_q$  in cyan based upon  $N_{ex}/N_i = 0.0674 + 0.0397\rho$ , the simplest way to account for a value of 0.06–0.07 for room-temperature/pressure gas [4] and the highest fit value for LXe at the highest  $E$ s in LXe, 0.20 [5]. That linear dependence of  $N_{ex}/N_i$  on  $\rho$  also serves to flatten the curvature of the  $W$  dependence, allowing for a linear fit, though with densities between 0.5 and 1 still “bulging” past the line (NEST previously utilized a sigmoid but abandoned it for simplicity, given the unknown errors on the data and an *ad hoc* exciton-ion ratio dependency.) Middle: the same corrected data repeated in cyan and same fit, but with data from condensed Xe (liquid and solid) added as solid circles. The only known data point for solid Xe [6] is the lowest / right-most, at an unknown  $\rho$  (taken to be 3.41 [7], but with an uncertainty spanning 3.1–3.64). The high- $W_q$  point above 3 g/cm<sup>3</sup> without an error is part of the same [2] data set as the GXe points. A new two-point fit to only LXe data points, those agreeing on a higher  $W_q$  near 2.88 averaged together, and the single point at 3.06, is introduced as a solid cyan line (the original repeated as a dashed line). Due to the uncertainty in the normalization of the hollow circles (GXe) the new steeper line may still agree with them. Right: A blow-up of LXe data points, with all high- $W_q$  points below 3 g/cm<sup>3</sup> that were merged (error-weighted average) into one point in the middle plot now separated, broken down by source in the legend: pink [6], red [8], orange [9], yellow [4; 10; 11; 12]. The remaining, from top to bottom, are: [2; 5; 13; 14; 15; 16; 17; 18; 19].

A reduction in  $W_q$  with density and between the gaseous and condensed phases is observed in nearly all noble elements [1], meaning it takes less  $E$  to either excite or ionize atoms as they get closer together. Additionally,  $N_{ex}/N_i$  appears to increase with  $\rho$ . This suggests that as mass density increases ionization density does as well, and recombination becomes stronger, resulting in a component of it that is near-immediate and can be modeled as direct excitation. This is known as Onsager or geminate recombination, and is effectively the opposite of volume or columnar recombination [20]. Another possibility, as mentioned in Section 2.2, is that  $W_i$  and  $W_{ex}$  must be considered separately. That would complicate the definition of a combined- $E$  scale for energy reconstruction, useful for any phase. It relies on strict anti-correlation.

Next, we cover the Fano-like factor  $F_q$  for variation in total quanta in greater depth than in the main body of the text, plus the excitation / recombination fluctuations again. For the former, the origins of its density, field, and  $E$  dependences are presented in Figure S2 from left to right. Resolution here is defined as Gaussian width divided by median. The full width half max (FWHM) is used for the first plot, as that is how its data were originally reported, and standard deviation is used for the others. Results from  $^{137}\text{Cs}$  are displayed, one of the most common past standard candles after  $^{57}\text{Co}$ . Xe gas and supercritical fluid at room temperature but distinct pressures are represented in the left pane (up to  $> 60$  bar, corresponding to about  $1.8 \text{ g/cm}^3$ ) while the other two are for liquid, where the standard NEST recombination fluctuations for LXe ( $\sigma_p = 0.04\text{--}0.09$ ) are applied, dependent on  $\mathcal{E}$  and  $E$ .

The recombination fluctuations, which become canceled out on a combined- $E$  scale, were historically often conflated with  $F_q$ . Effective  $F_{ph}$  and  $F_{e-}$  (aka  $F_{sc}$  and  $F_i$ ) can still be defined, with enormous but inconsequential values: 60 and 20 for the  $^{137}\text{Cs}$  example, at 1000 V/cm in LXe, matching [21].

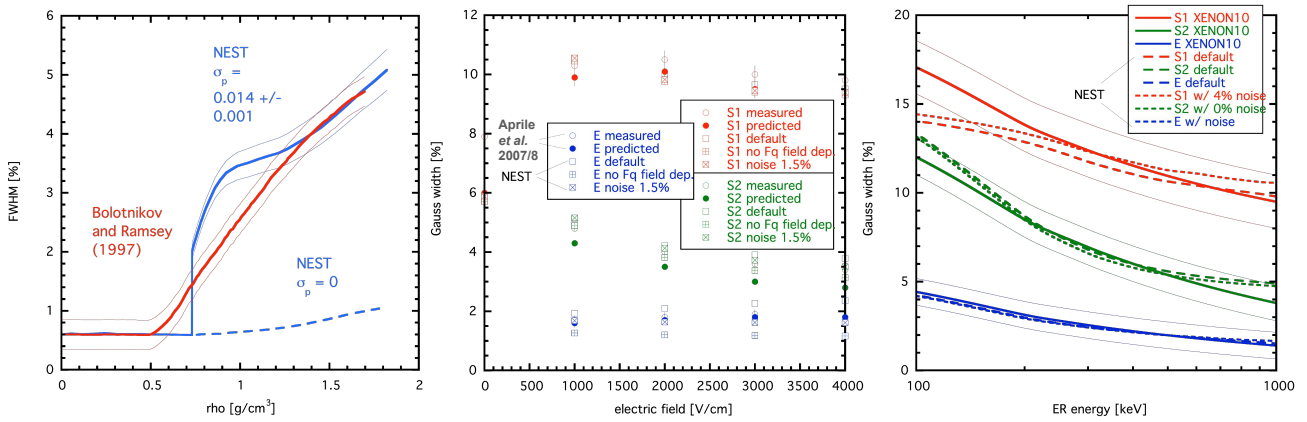


**Figure S2.** Left: The ionization-only resolution of  $^{137}\text{Cs}$  gamma rays in GXe at 7 kV/cm vs. density [2] in red, with approximate error band (note: these same data feature prominently in [21]). At very low densities there is nearly no recombination: S1 comes only from excitations at this very high field, but  $N_{ex}/N_i$  is low too (near 0.06). Thus, resolution in this flat region is driven almost exclusively by low  $F_q = 0.1 - 0.2 \lesssim F_i$ . To follow  $F$ 's  $\rho$  dependence, featured in Eq. (7) in the main text, a cubic spline was fit to discrete  $F$ 's measured or predicted (calculated) for xenon as a low-pressure gas, supercritical fluid, liquid, and solid, featured in Table 2.4 of [1]. NEST (cyan) was intentionally not fit to the red, to see if it could be predicted. As a result it does not quite agree on the  $\rho$  at which resolution begins to depart from flatness, at  $O(100)$  bar, and has some disagreement at moderate  $\rho$ s (though no actual major experiments operate under such conditions any longer). The dashed cyan line represents only binomial recombination fluctuations, with the closest fit to real data achieved with a non-zero value of the non-binomial contribution (solid lines) thus demonstrating that these matter even in a gas or a van der Waals fluid not just true liquid, at sufficiently high densities. Energy resolution is not driven by just  $F_q$ , when considering only a single channel such as ionization alone. Middle: Resolution as a function of  $\mathcal{E}$  for LXe ( $2.9 \text{ g/cm}^3$ ) for the same fixed  $E = 662$  keV and particle ( $\gamma$ ) again, for both ionization (S2, green) and scintillation (S1, red) now, as well as for the combined- $E$  scale (blue) that merges the information from both to create the best-possible resolution / lowest width [22]. Default NEST options reproduce real data well, but without the  $F_q$  square-root  $\mathcal{E}$  dependence from Eqn. (7) in the text the final resolution is seriously underestimated: 1.1–1.2 compared to 1.5–2.0% in reality. Another option for matching data with NEST is presented where  $F_q \approx 0$  and linear noise terms are added to represent unknown detector effects, which the “predicted” points from Aprile were meant to address. In all NEST options presented,  $g_1 = 0.05$ , typical for the time of data collection, and 40 V/cm stands in for 0 V/cm (impossible to directly model within NEST, as explained in the text). Note that [2] also has LXe data, and found 2.9% (converted from FWHM) resolution at 7000 V/cm, in good agreement with the asymptotic behavior of the S2s seen in this plot. Right: With density (LXe) and field (730 V/cm) both fixed now this is the  $E$  dependence, for XENON10 [15]. Two NEST options are presented: the default, plus usage of Gaussian noise terms again, at  $F_q = 0.03$  (no  $\mathcal{E}$  nor  $E$  dependence, only  $\rho$ ). At 662 keV, the measured S1, S2, and total ( $E$ ) resolutions were 10.8, 5.1, and 2.2%, respectively, all comparable to the 1 kV/cm results from the middle plot.

## 2 APPENDIX B: TABULATION OF NEST MODEL PARAMETERS

In this appendix, we provide tables detailing the functions and model parameters used in NEST for LXe yields from  $\beta$  ER,  $\gamma$  ER, NR, as well as their fluctuations. NEST has additional models for  $^{83m}\text{Kr}$  ER as well as NR from non-Xe nuclei (including  $\alpha$  decay), findable in code on GitHub [23].

**Table S1.** Table of NEST model parameters comprising the  $\beta$  ER yield models for charge, as shown in Equation (5), and light.

$m_1$	Stitching-region yield for $\beta$ ER charge yields between low and high energies, depending on field and density: $m_1 = 30.66 + (6.20 - 30.66)/(1 + (\mathcal{E}/73.86)^{2.03})^{0.42}$ at a typical LXe density. Takes values $\mathcal{O}(10 \text{ keV}^{-1})$ for $\mathcal{O}(100 \text{ V/cm})$ fields.
$m_2$	Low-energy asymptote of the $\beta$ ER charge yield equation. Default value is approximately $77.3 \text{ keV}^{-1}$ .
$m_3$	Controls the energy-dependent shape of the $\beta$ charge yields in the low-energy (Thomas-Imel) regime: $m_3 = \log_{10}(\mathcal{E}) \cdot 0.14 + 0.53$ . Field-dependent function, with values of approximately 0.8-1.5 keV for $\mathcal{O}(100 \text{ V/cm})$ fields.
$m_4$	Field-dependent control on the energy-dependent shape of the $\beta$ charge yields at lower energies: $m_4 = 1.82 + (2.83 - 1.82)/(1 + (\mathcal{E}/144.65)^{-2.81})$ . Takes values from approximately 2.0-2.8 for $\mathcal{O}(100 \text{ V/cm})$ fields.
$m_5$	High-energy asymptote of the $\beta$ charge yield model. Defined as: $m_5 = \frac{1}{W} \cdot [1 + N_{ex}/N_i]^{-1} - m_1$ (See Ref. [24].)
$m_6$	Low-energy asymptote of the higher-energy behavior for $\beta$ ER charge yields. Degenerate with $m_1$ and explicitly set to $0 \text{ keV}^{-1}$ .
$m_7$	Field-dependent scaling on the behavior of the $\beta$ charge yields at higher energies: $m_7 = 7.03 + (98.28 - 7.03)/(1 + (\mathcal{E}/256.48)^{1.29})$ . Takes values $\mathcal{O}(10 \text{ keV})$ for $\mathcal{O}(100 \text{ V/cm})$ fields.
$m_8$	Control on the energy-dependent shape of the $\beta$ charge yields at higher energies. The default value is a constant, 4.3.
$m_9$	Asymmetry control on the low-energy behavior. The default value is a constant, 0.3.
$m_{10}$	Asymmetry control on the high-energy behavior of the $\beta$ charge yields model: $m_{10} = 0.05 + (0.12 - 0.05)/(1 + (\mathcal{E}/139.26)^{-0.66})$ . Field-dependent function that takes values $\sim 0.1$ for $\mathcal{O}(100 \text{ V/cm})$ fields.

**Table S2.** Table of NEST model parameters comprising the  $\gamma$  ER yield models for light and for charge, reusing Equation (5) from the  $\beta$  ER yields.

$m_1$	Field-dependent function controlling the transition between lower and higher energies: $m_1 = 34.0 + (3.3 - 34.0)/(1 + (\mathcal{E}/165.3)^{0.7})$ .
$m_2$	Low-energy asymptote of the $\gamma$ ER charge yield equation, defined as $1/W_q$ in units of $\text{keV}^{-1}$ .
$m_3$	Controls the energy-dependent shape of the $\gamma$ charge yields in the low-energy (Thomas-Imel) regime; a constant value of 2 keV is used.
$m_4$	Control on the energy-dependent shape of the $\gamma$ charge yields at lower energies; a constant power of 2 is used.
$m_5$	High-energy asymptote of the $\gamma$ charge yield model. Defined as: $m_5 = 23.2 + (10.7 - 23.1)/(1 + (\mathcal{E}/34.2)^{0.9})$ .
$m_6$	Low-energy asymptote of the higher-energy behavior for $\gamma$ ER charge yields. Degenerate with $m_1$ and explicitly set to $0 \text{ keV}^{-1}$ .
$m_7$	Field-dependent and density-dependent scaling on the behavior of the $\gamma$ charge yields at higher energies: $m_7 = 66.8 + (829.3 - 66.8)/(1 + (\rho^{8.2} \cdot \mathcal{E}/(2.4 \cdot 10^5))^{0.8})$ .
$m_8$	Control on the energy-dependent shape of the $\gamma$ charge yields at higher energies. Default value is a constant power of 2.
$m_9$	Asymmetry control on the low-energy behavior: unused for $\gamma$ ER yields and set to unity.
$m_{10}$	Asymmetry control on the high-energy behavior of the $\gamma$ charge yields model: unused for $\gamma$ ER yields and set to unity.

**Table S3.** Table of NEST model parameters comprising the NR mean yield models: for total quanta, charge, and light, as shown in Equations (9), (12), and (13).

$a$	Scaling on NR total quanta. Default value is $11_{-0.5}^{+2.0} \text{ keV}^{-b}$ .
$b$	Power-law exponent for the NR total quanta. Default value is $1.1 \pm 0.05$ .
$\varsigma$	Field dependence in NR light and charge yields, with mass-density-dependent scaling (Equation (11)).
$\rho_0$	Reference density for scaling density-dependent NEST functions: $2.90 \text{ g/cm}^3$ .
$v$	Hypothetical exponential control on density dependence in $\varsigma$ ; the default value is 0.3.
$\gamma$	Power-law base for the field dependence in $\varsigma$ . Default value is $0.0480 \pm 0.0021$ .
$\delta$	Power-law exponent in the field dependence in $\varsigma$ ; default value is $-0.0533 \pm 0.0068$ .
$\epsilon$	Reshaping parameter for NR charge yields, controlling the effective energy scale at which the charge yield behavior changes. The default value is $12.6_{-2.9}^{+3.4} \text{ keV}$ .
$p$	Exponent which controls the shape of the energy dependence of the NR charge yields at energies greater than $\mathcal{O}(\epsilon)$ . Default value is 0.5.
$\zeta$	Controls the energy dependence of the NR charge yields roll-off at low energies. Default value is $0.3 \pm 0.1 \text{ keV}$ .
$\eta$	Controls energy-dependent shape of the NR charge yields roll-off at low energies. Default value is $2 \pm 1$ .
$\theta$	Controls the energy dependence of the NR light yields roll-off. Default value is $0.30 \pm 0.05 \text{ keV}$ .
$\iota$	Controls the shape of the energy dependence of the NR light yields roll-off. Default value is $2.0 \pm 0.5$ .

**Table S4.** Table of NEST model parameters for different types of fluctuations for ERs and NRs.

$F_q$	Fano-like factor for statistical fluctuations. For ERs, this is proportional to $\sqrt{E} \cdot \mathcal{E}$ ; see Equation (7). For NRs, this is separated into fluctuations for $N_{ex}$ and $N_i$ ; the default value is 0.4 for both in NEST v2.3.11, while the values were 1.0 in previous NEST versions. ( $F_{ex}$ was underestimated to be conservative for low-mass WIMPs.)
$\sigma_p$	Non-binomial contribution to recombination fluctuations, modeled as a skew Gaussian in electron fraction space.
$A$	Amplitude of non-binomial recombination skew Gaussian. For NRs, this is a constant 0.04 (v2.3.11) or 0.1 (v2.3.10). For ERs, it is field-dependent: $A = 0.09 + (0.05 - 0.09)/(1 + (\mathcal{E}/295.2)^{251.6})^{0.007}$ , where 0.05 was 0.055 in 2.3.10
$\xi$	Centroid-location parameter of the non-binomial recombination skew Gaussian. Default value for ERs is an electron fraction of 0.45, but 0.5 for NRs.
$\omega$	Width parameter for the non-binomial recombination skew Gaussian. Takes value of 0.205 for ERs and 0.19 for NRs.
$\alpha_p$	Skewness parameters for the non-binomial recombination skew Gaussian. Takes the value -0.2 for ERs, while being zero for NRs.
$\alpha_r$	Additional skewness in the recombination process itself. Field- and energy- dependent equations can be found in Ref. [25] for ERs, while this is fixed at 2.25 for NRs, with evidence of higher values in [25].

## REFERENCES

- Aprile E, Bolotnikov AE, Bolozdynya AL, Doke T. *Noble Gas Detectors* (Wiley) (2008). doi:10.1002/9783527610020.
- Bolotnikov A, Ramsey B. The spectroscopic properties of high-pressure xenon. *Nuclear Instruments and Methods in Physics Research Section A: Accelerators, Spectrometers, Detectors and Associated Equipment* **396** (1997) 360–370. doi:http://dx.doi.org/10.1016/S0168-9002(97)00784-5.
- Ahlen SP. Theoretical and experimental aspects of the energy loss of relativistic heavily ionizing particles. *Rev. Mod. Phys.* **52** (1980) 121–173. doi:10.1103/RevModPhys.52.121.
- Miyajima M, Takahashi T, Konno S, Hamada T, Kubota S, Shibamura H, et al. Average energy expended per ion pair in liquid argon. *Phys. Rev. A* **9** (1974) 1438–1443. doi:10.1103/PhysRevA.9.1438.

- Doke T, Hitachi A, Kikuchi J, Masuda K, Okada H, Shibamura E. Absolute scintillation yields in liquid argon and xenon for various particles. *Japanese Journal of Applied Physics* **41** (2002) 1538–1545. doi:10.1143/jjap.41.1538.
- Obodovskii IM, Pokachalov SG. (in Russian). *Soviet Journal of Low Temp. Phys.* **5** (1974) 829–836.
- Yoo J, Cease H, Jaskierny W, Markley D, Pahlka R, Balakishiyeva D, et al. Scalability Study of Solid Xenon. *JINST* **10** (2015) P04009. doi:10.1088/1748-0221/10/04/P04009.
- Takahashi T, Konno S, Hamada T, Miyajima M, Kubota S, Nakamoto A, et al. Average energy expended per ion pair in liquid xenon. *Phys. Rev. A* **12** (1975) 1771–1775. doi:10.1103/PhysRevA.12.1771.
- Obodovskii IM, Pokachalov SG. (in Russian). *Soviet Journal of Low Temp. Phys.* **5** (1979) 393.
- Doke T, Masuda K, Shibamura E. Estimation of absolute photon yields in liquid argon and xenon for relativistic (1 MeV) electrons. *NIM A* **291** (1990) 617–620.
- Doke T. A historical view on the R&D for liquid rare gas detectors. *NIM A* **327** (1993) 113–118. doi:https://doi.org/10.1016/0168-9002(93)91423-K.
- Tanaka M, Doke T, Hitachi A, Kato T, Kikuchi J, Masuda K, et al. LET dependence of scintillation yields in liquid xenon. *NIM A* **457** (2001) 454–463. doi:https://doi.org/10.1016/S0168-9002(00)00785-3.
- Shutt T, Dahl C, Kwong J, Bolozdynya A, Brusov P. Performance and fundamental processes at low energy in a two-phase liquid xenon dark matter detector. *NIM A* **579** (2007) 451–453. doi:https://doi.org/10.1016/j.nima.2007.04.104. Proceedings of the 11th Symposium on Radiation Measurements and Applications.
- Dahl CE. *The physics of background discrimination in liquid xenon, and first results from XENON10 in the hunt for WIMP dark matter*. Ph.D. thesis, Princeton University (2009).
- E Aprile *et al.* Design and performance of the XENON10 dark matter experiment. *Astroparticle Physics* **34** (2011) 679 – 698. doi:https://doi.org/10.1016/j.astropartphys.2011.01.006.
- Horn M, et al. Nuclear recoil scintillation and ionisation yields in liquid xenon from ZEPLIN-III data. *Physics Letters B* **705** (2011) 471–476. doi:10.1016/j.physletb.2011.10.038.
- Goetzke L, Aprile E, Anthony M, Plante G, Weber M. Measurement of light and charge yield of low-energy electronic recoils in liquid xenon. *Phys. Rev. D* **96** (2017) 103007.
- Anton G, et al. Measurement of the scintillation and ionization response of liquid xenon at MeV energies in the EXO-200 experiment. *Phys. Rev. C* **101** (2020) 065501. doi:10.1103/PhysRevC.101.065501.
- Baudis L, Sanchez-Lucas P, Thieme K. A measurement of the mean electronic excitation energy of liquid xenon. *The Eur. Phys. Journal C* **81** (2021) 1060. doi:10.1140/epjc/s10052-021-09834-x.
- Nygren DR. Columnar recombination: a tool for nuclear recoil directional sensitivity in a xenon-based direct detection WIMP search. *Journal of Physics: Conference Series* **460** (2013) 012006. doi:10.1088/1742-6596/460/1/012006.
- Nygren D. High-pressure xenon gas electroluminescent TPC for zero-neutrino double-beta-decay search. *NIM A* **603** (2009) 337–348. doi:https://doi.org/10.1016/j.nima.2009.01.222.
- Aprile E, Giboni KL, Majewski P, Ni K, Yamashita M. Observation of anticorrelation between scintillation and ionization for MeV gamma rays in liquid xenon. *Phys. Rev. B* **76** (2007) 014115. doi:10.1103/PhysRevB.76.014115.
- [Dataset] Szydagis M, et al. Noble Element Simulation Technique <https://zenodo.org/records/8215927> (2023). doi:10.5281/zenodo.8215927.
- Akerib DS, et al. Improved modeling of beta electronic recoils in liquid xenon using LUX calibration data. *Journal of Instrumentation* **15** (2020a) T02007. doi:10.1088/1748-0221/15/02/t02007.
- Akerib DS, et al. Discrimination of electronic recoils from nuclear recoils in two-phase xenon time projection chambers. *Phys. Rev. D* **102** (2020b) 112002. doi:10.1103/PhysRevD.102.112002.